Monthly Notices of the ROYAL ASTRONOMICAL SOCIETY

MNRAS **531,** 1409–1421 (2024)
Advance Access publication 2024 May 15

https://doi.org/10.1093/mnras/stae1263

Tidal disruption events from three-body scatterings and eccentricity pumping in the discs of active galactic nuclei

Chaitanya Prasad,[1]★ Yihan Wang [2,3] Rosalba Perna,[1,4] K. E. Saavik Ford [4,5,6] and Barry McKernan [4,5,6]

[1]*Department of Physics and Astronomy, Stony Brook University, Stony Brook, NY 11794-3800, USA*
[2]*Nevada Center for Astrophysics, University of Nevada, Las Vegas, NV 89154, USA*
[3]*Department of Science, BMCC, City University of New York, New York, NY 10007, USA*
[4]*Department of Physics and Astronomy, University of Nevada Las Vegas, Las Vegas, NV 89154, USA*
[5]*Center for Computational Astrophysics, Flatiron Institute, 162 5th Ave, New York, NY 10010, USA*
[6]*Department of Astrophysics, American Museum of Natural History, New York, NY 10024, USA*

Accepted 2024 May 9. Received 2024 May 3; in original form 2023 September 26

ABSTRACT

Tidal disruption events (TDEs) are routinely observed in quiescent galaxies, as stars from the nuclear star cluster are scattered into the loss cone of the central supermassive black hole (SMBH). TDEs are also expected to occur in active galactic nuclei (AGNs), due to scattering or orbital eccentricity pumping of stars embedded in the innermost regions of the AGN accretion disc. Encounters with embedded stellar-mass black holes (BH) can result in AGN μTDEs. AGN TDEs and μTDEs could therefore account for a fraction of observed AGN variability. Here, by performing scattering experiments with the few-body code `SpaceHub`, we compute the probability of AGN TDEs and μTDEs as a result of 3-body interactions between stars and binary BHs. We find that AGN TDEs are more probable during the early life of the AGNs, when rates are $\sim (6 \times 10^{-5} - 5 \times 10^{-2})(f_\bullet/0.01)\,\mathrm{AGN}^{-1}\,\mathrm{yr}^{-1}$ (where $f_\bullet$ is the ratio between the number density of BHs and stars), generally higher than in quiescent galactic nuclei. By contrast, μTDEs should occur throughout the AGN lifetime at a rate of $\sim (1 \times 10^{-4} - 4 \times 10^{-2})(f_\bullet/0.01)\,\mathrm{AGN}^{-1}\,\mathrm{yr}^{-1}$. Detection and characterization of AGN TDEs and μAGN TDEs with future surveys using *Rubin* and *Roman* will help constrain the populations of stars and compact objects embedded in AGN discs, a key input for the LVK AGN channel.

Key words: accretion, accretion discs – black hole physics – galaxies: active.

1 INTRODUCTION

Tidal disruption events (TDEs) occur when a star passes close enough to a supermassive black hole (SMBH) to be disrupted. Around half of the resulting stellar debris self-collides and accretes onto the SMBH (Rees 1988; Phinney 1989). TDEs are widely used to probe distributions of SMBH mass and spin in the local Universe (e.g. van Velzen 2018; Stone et al. 2020), but can also be used to test general relativity (e.g. Ryu et al. 2020), or even light axion models (Du et al. 2022). TDEs are routinely discovered in quiescent galactic nuclei (see Gezari 2021 for a comprehensive observational review). However there is increased recent interest in their likely presence in active galactic nuclei (AGNs).

AGNs are powered by the accretion of gas discs onto SMBH. Star formation within the AGN disc adds stars and compact objects directly (e.g. Goodman & Tan 2004; Levin 2007; Dittmann & Miller 2020). Since SMBH are also orbited by nuclear star clusters (NSCs) (e.g. Neumayer, Seth & Böker 2020), a fraction of the NSC must become embedded in the AGN disc, adding to the embedded population over time (e.g. Artymowicz, Lin & Wampler 1993; Fabj et al. 2020; Nasim et al. 2023; Wang et al. 2023b). Objects from this embedded population will experience gas torques, migrate, and dynamically encounter each other, leading to collisions, scatterings, and mergers (Bellovary et al. 2016; Secunda et al. 2019; Tagawa et al. 2020, 2021a, b). Binary BH mergers in AGN discs should be detected in gravitational waves by LIGO/Virgo (e.g. McKernan et al. 2014; Bartos et al. 2017; Stone, Metzger & Haiman 2017; Ford & McKernan 2022). The LIGO/Virgo AGN channel may account for (among other things): unusual gravitational wave events (e.g. Abbott et al. 2020a, b), the asymmetric $\chi_{\rm eff}$ distribution (Wang et al. 2021c) (unexpected for a dynamics channel), and the intriguing anticorrelation in the (q, $\chi_{\rm eff}$) distribution (Callister et al. 2021; McKernan et al. 2022a).

AGN discs are therefore expected to contain an embedded stellar population, which may evolve quite differently from stars in vacuo (Cantiello, Jermyn & Lin 2021; Dittmann, Cantiello & Jermyn 2021; Jermyn et al. 2021; Perna et al. 2021b). Complicated dynamical interactions among the embedded populations allow for the possibility of embedded TDEs around the central SMBH (e.g. McKernan et al. 2022b), as well as TDEs by stellar-mass BHs within the disc (Yang et al. 2022). TDEs by embedded BH, also known as μTDEs (Perets et al. 2016), are expected to release energy in a shorter lived but more intense outburst than standard TDEs (Kremer et al. 2019; Wang,

★ E-mail: chaitanya.prasad@stonybrook.edu

Perna & Armitage 2021a). Certainly the rich (chaotic) dynamics inherently involved in three-body encounters in AGN discs should lead us to expect a wide range of possible outcomes, including TDEs and μTDEs (Lopez Martin et al. 2019; Ryu, Perna & Wang 2022; Ryu et al. 2023a, b, 2024a; Xin et al. 2024).

AGNs are inherently variable, with a large number of potential sources of variability on different time and energy scales. A growing number of AGNs show an extreme degree of variability (Graham et al. 2017), flaring or apparently changing their accretion state over timescales incompatible with standard accretion disc models (Dexter & Begelman 2018). Many mechanisms have been proposed to explain extreme AGN flaring, including: microlensing (Hawkins 1993), obscuration changes (Nenkova et al. 2008; Elitzur 2012), nearby supernovae (Kawaguchi et al. 1998), disc instabilities (Penston & Perez 1984; Shapovalova et al. 2010; Elitzur, Ho & Trump 2014), disc fronts (Noda & Done 2018; Stern et al. 2018), or magnetically launched winds (Cannizzaro et al. 2020). TDEs in AGN could provide (yet) another natural explanation (Eracleous et al. 1995; Merloni et al. 2015; Blanchard et al. 2017), in some fraction of cases. Qualitative estimates of AGN TDE light curves were initially investigated by McKernan et al. (2022b) and predicted signatures may have been observed (Cannizzaro et al. 2022). AGN TDEs could therefore be an excellent mechanism to study population dynamics in AGN discs as well as the properties of the discs themselves.

Dynamical interactions may contribute to obtaining TDEs and μTDEs in AGN discs. Stars scattering off stellar mass BHs in an AGN disc might be sent onto a path towards the SMBH, or be tidally disrupted by the scattering BH itself. The former scenario is especially favoured during the early times of an AGN, when the stars from the NSC become instantaneously embedded in the disc upon the AGN turns on, and about half of them will find themselves in retrograde orbits within the disc. Due to drag, these become highly eccentric, which are then easily driven onto the SMBH (Secunda et al. 2021; McKernan et al. 2022b).

While previous dynamical work on the fate of post-scattered stars has largely focused on scattering with individual BHs (Wang et al. 2023b), here we focus our study on strong dynamical encounters with BH binaries, given their importance in AGN discs (Samsing et al. 2022). This is interesting to study both due to the fact that binaries have a larger geometric cross-section than single stars, as well as because binary formation is enhanced in AGN discs (and hence the star and compact object population is different than that in NSCs). By performing detailed scattering experiments in various regions of the disc, we aim to identify regions of parameter space in which BH binary scatterings lead to either a TDE by the SMBH, or a μTDE by the BH binary itself.

The paper is organized as follows: In Section 2 we evaluate whether the AGN disc can remain in a state of full loss cone, to inform us on the proper initial conditions for the scattering experiments. These are described in Section 3, together with our numerical methods. Our results are presented in Section 4, and we summarize and discuss their astrophysical implications in Section 5.

2 TIDAL DISRUPTION EVENTS AROUND SUPERMASSIVE BLACK HOLES

In the following we will discuss the main dynamical processes responsible for loss cone refilling, beginning with the standard case of TDEs from stars in the NSC around the SMBH of a quiescent galaxy (Section 2.1), and then specializing to the case of AGN discs (Section 2.2).

2.1 TDEs in nuclear star clusters

As long as orbiting stars in NSCs possess sufficient angular momentum (L) they avoid close passes of the SMBH and tidal disruption. TDEs will not occur if $L > L_{\rm min} \sim \sqrt{G M_{\rm SMBH} R_{\rm TDE}}$, where

$$R_{\rm TDE} = \left(\frac{M_{\rm SMBH}}{M_*}\right)^{1/3} R_* \tag{1}$$

is the tidal disruption radius of the star of mass M_* and radius R_*, and $M_{\rm SMBH}$ is the mass of the SMBH. TDEs remove stellar orbits from the 'loss cone' ($L < L_{\rm min}$), while relaxation processes (two-body scattering) within the NSC add stars stochastically to the loss cone.

2.1.1 Two-body relaxation

Stars within the radius of influence of the SMBH (r_h) exhibit approximately Keplerian motion, where (Merritt 2013)

$$r_h \sim \frac{G M_{\rm SMBH}}{\sigma^2_{\rm NSC}} = 10.75 \left(\frac{M_{\rm SMBH}}{10^8 M_\odot}\right) \left(\frac{\sigma_{\rm NSC}}{200\ {\rm km\ s^{-1}}}\right)^{-2} {\rm pc}\,, \tag{2}$$

and $\sigma_{\rm NSC}$ is the velocity dispersion of the star cluster. Although the SMBH gravitational potential dominates, the potential due to the stars induces stellar orbital precession. The energy and angular momentum of individual stars therefore fluctuate on a relaxation time, $t_{\rm rel}$, given by (Jeans 1913, 1916; Chandrasekhar 1942; Binney & Tremaine 1987):

$$\frac{\Delta E}{E} \sim \sqrt{\frac{t}{t_{\rm rel}}}\,, \tag{3}$$

$$\frac{\Delta L}{L_{\rm max}(E)} \sim \sqrt{\frac{t}{t_{\rm rel}}}\,. \tag{4}$$

Here, $t_{\rm rel} = \frac{M^2_{\rm SMBH}}{M^2_* N \ln\Lambda} T$, where N is the number of stars within the NSC, $\ln\Lambda$ is the Coulomb logarithm, T is the star's orbital period, and $L_{\rm max} \sim \sqrt{G M_{\rm SMBH} a}$, with a the semimajor axis of the star's orbit.

A stellar orbit within the loss cone is consumed by the SMBH during a single orbital period, while the relaxation process introduces fluctuations in angular momentum given by

$$\Delta L_{\rm orb} \sim L_{\rm max}(E) \sqrt{\frac{\log(\Lambda) m^2 N}{M^2_{\rm SMBH}}}\,. \tag{5}$$

When $\Delta L_{\rm orb} \gg L_{\rm min}$, loss-cone refilling due to relaxation is faster than the consumption of stars in TDEs. This is the 'full loss cone' regime, where the equilibrium TDE rate for a given E is determined by the loss cone size. L is larger on the outskirts of the NSC, so the outer region of the NSC is in the full loss cone regime and this dominates the overall TDE rate in NSCs.

The TDE rate for a given energy E can be expressed using the dimensionless number $\lambda(E)$, which represents the fraction of stars with that particular energy E that undergo disruption per orbital period. In the full loss cone regime (Frank & Rees 1976; Lightman & Shapiro 1977; Rees 1988; Magorrian & Tremaine 1999; Merritt & Poon 2004; Stone & Metzger 2016),

$$\lambda_{\rm full}(E) \sim \frac{\Delta L^2_{\rm min}}{L^2_{\rm max}(E)}\,. \tag{6}$$

The overall TDE rate of the NSC is then

$$\dot{N}_{\rm TDE} \sim \int_{r_c}^{r_h} \frac{\lambda_{\rm full}(E)}{T} n(r) r^2 {\rm d}\Omega {\rm d}r\,, \tag{7}$$

where r_c represents the critical radius where $\Delta L_{\rm orb} = L_{\rm min}$, i.e. the inner boundary of the full loss cone regime, and $N(E)$ is the number

of energy states. The overall TDE rate falls within the range of 10^{-4} to 10^{-6} yr^{-1} for SMBHs with typical masses ranging from 10^6 to $10^{10}\,M_\odot$, and NSCs with energy profiles that scale approximately as $\frac{\mathrm{d}N(E)}{\mathrm{d}r} \propto r^0$ to r^1.

Additional effects, such as resonant relaxation (Rauch & Tremaine 1996; Rauch & Ingalls 1998; Hopman & Alexander 2006; Kocsis & Tremaine 2011; Hamers et al. 2018) can provide an additional source of TDEs, particularly in nearly empty loss cones. However, in most NSCs this is a sub-dominant effect and we do not consider it further here.

2.2 TDEs in AGN discs

In AGN discs, the population of stellar orbits in the energy–angular momentum ($E-L$) phase space is influenced by several processes, and the population of stellar orbits at the loss-cone boundary is a crucial factor determining the overall TDE rate.

In the following, we adopt an α-disc model (Shakura & Sunyaev 1973). This can be parametrized in terms of the viscosity parameter α_d, the accretion rate efficiency λ_d, and the Toomre parameter Q_d. The accretion rate can then be approximated as

$$\dot{M} = 2.2\lambda_d \left(\frac{M_{\rm SMBH}}{10^8 \mathrm{M}_\odot}\right) \mathrm{M}_\odot\,\mathrm{yr}^{-1}\,, \tag{8}$$

and the surface density follows as

$$\Sigma = \frac{\dot{M}}{2\pi r v_r}\,, \tag{9}$$

where

$$v_r = \alpha_d h^2 \sqrt{\frac{GM_{\rm SMBH}}{r}}\,, \tag{10}$$

with $h \equiv H/r$. The scale height H of the disc is given by

$$H = \left(\frac{Q_d \dot{M}}{2\alpha_d M_{\rm SMBH}\Omega_d}\right)^{1/3} r\,, \tag{11}$$

where r is the distance from the SMBH, and $\Omega_d = v_r/r$ is the orbital frequency.

2.2.1 *Eccentricity damping due to co-orbital gas*

Prograde stellar orbits in AGN discs experience torques from co-orbiting gas, which causes damping of their orbital eccentricity. A similar process acts on planets embedded in protoplanetary discs (Goldreich & Sari 2003). The damping time-scale is (Tanaka & Ward 2004; Arzamasskiy, Zhu & Stone 2018)

$$\begin{aligned} t_{\rm e,damp} &\sim h^2 \frac{M_{\rm SMBH}}{\Sigma\pi r^2}\frac{M_{\rm SMBH}}{M_*} T = Q_d h \frac{M_{\rm SMBH}}{M_*} T \\ &= 0.42 Q_d^{4/3} \left(\frac{\lambda_d}{\alpha_d}\right)^{1/3} \left(\frac{r}{1000\mathrm{au}}\right)^2 \left(\frac{M_*}{1M_\odot}\right)^{-1} \\ &\quad \left(\frac{M_{\rm SMBH}}{10^8 M_\odot}\right)^{1/3} \mathrm{Myr}\,. \end{aligned} \tag{12}$$

Due to eccentricity damping, fully embedded *prograde* orbits tend to reach their maximum angular momentum for a given orbital energy, which pushes the orbits away from the loss cone.

2.2.2 *Refilling of disc stars from the NSC*

In addition to the initially fully embedded prograde orbits, the interaction between the disc and the NSC results in the capture of stars from the NSC into the AGN disc. These captured stars refill the $E-L$ phase space, providing extra relaxation for orbits within the AGN disc. The capture process is characterized by a typical time-scale (Generozov & Perets 2023; Wang, Zhu & Lin 2024)

$$\begin{aligned} t_{\rm cap} \sim \frac{\Sigma_*}{\Sigma} T = \; & 0.7 Q_d^{2/3} \left(\frac{\alpha_d}{\lambda_d}\right)^{1/3} \left(\frac{M_*}{1M_\odot}\right) \left(\frac{M_{\rm SMBH}}{10^8 M_\odot}\right)^{-4/3} \\ & \left(\frac{R_*}{R_\odot}\right)^{-2} \left(\frac{r}{1000\mathrm{au}}\right)^3 \mathrm{Myr}\,, \end{aligned} \tag{13}$$

where $\Sigma_* = M_*/\pi R_*^2$ is the surface density of stars of radius R_*. The stellar refilling process from capture can be described as (Wang et al. 2024):

$$M_{\rm cap} \sim 2 M_{\rm SMBH} f_* \left(\frac{\Sigma}{\Sigma_*}\frac{t}{T_h}\right)^{1-\gamma_{\rm NSC}/3} \tag{14}$$

$$\frac{\mathrm{d}N}{\mathrm{d}r} \propto r^{-1/4}\,. \tag{15}$$

Here, $M_{\rm cap}$ is the total captured stellar mass in the AGN disc, f_* is the mass fraction of stars in the NSC, T_h is the orbital period at r_h, and $\gamma_{\rm NSC}$ is the radial number density profile power-law index of the NSC.

During the disc–star interactions, eccentricity damping drives captured stars (overwhelmingly prograde orbits) into nearly circular orbits. Thus, most captured stars populate the region near $L_{\rm max}$, which is far away from the loss cone. So the disc capture process is unable to efficiently refill the loss cone.

2.2.3 *Two-body relaxation from in-disc single-single scatterings*

Two-body relaxation (via close encounters and remote perturbations) could also relax the orbital angular momentum of disc stars away from $L_{\rm max}(E)$, potentially generating TDEs. However, the total number of stars in an AGN disc is a small fraction of the total number of stars in an NSC, yielding only small fluctuations in the $E-L$ phase space. The two-body relaxation time-scale in an AGN disc is approximately given by

$$\begin{aligned} t_{\rm rel,disc} &\sim \frac{v_{\rm orb}^2(a)}{\dot{v}_{\rm orb}^2(a)} \sim \frac{a^3}{\bar{b}(a)^3} T \\ &= 776 Q^{-2/3} \left(\frac{\lambda_d}{\alpha_d}\right)^{1/3} \left(\frac{M_*}{1M_\odot}\right)^{-1} \left(\frac{M_{\rm SMBH}}{10^8 M_\odot}\right)^{10/3} \\ &\quad \left(\frac{R_*}{R_\odot}\right)^2 \mathrm{Gyr}\,, \end{aligned} \tag{16}$$

where $\bar{b}(a)$ is the average impact parameter for scattering between two prograde circular orbits around semimajor axis a. Since $t_{\rm rel,\,disc} \gg t_{\rm e,\,damp}$ in equation (12), orbital eccentricity damping is much faster than the relaxation process. So in-disc two-body relaxation cannot efficiently fill the AGN loss cone with stellar orbits.

2.2.4 *TDE from retrograde orbits*

Approximately half of the initial orbits in a newly formed AGN disc will be retrograde with respect to the flow of the disc gas (McKernan et al. 2022b). Stars on these retrograde orbits will experience strong aerodynamic drag. In low density regions of the AGN disc, both the eccentricity and the semimajor axis of the star decrease. However, in specific AGN disc models with high density in the inner regions (e.g. the classic Shakura-Sunyaev disc; Shakura & Sunyaev 1973), the time-scale for semimajor axis decay can become shorter than the orbital period. In such cases, the eccentricity would increase

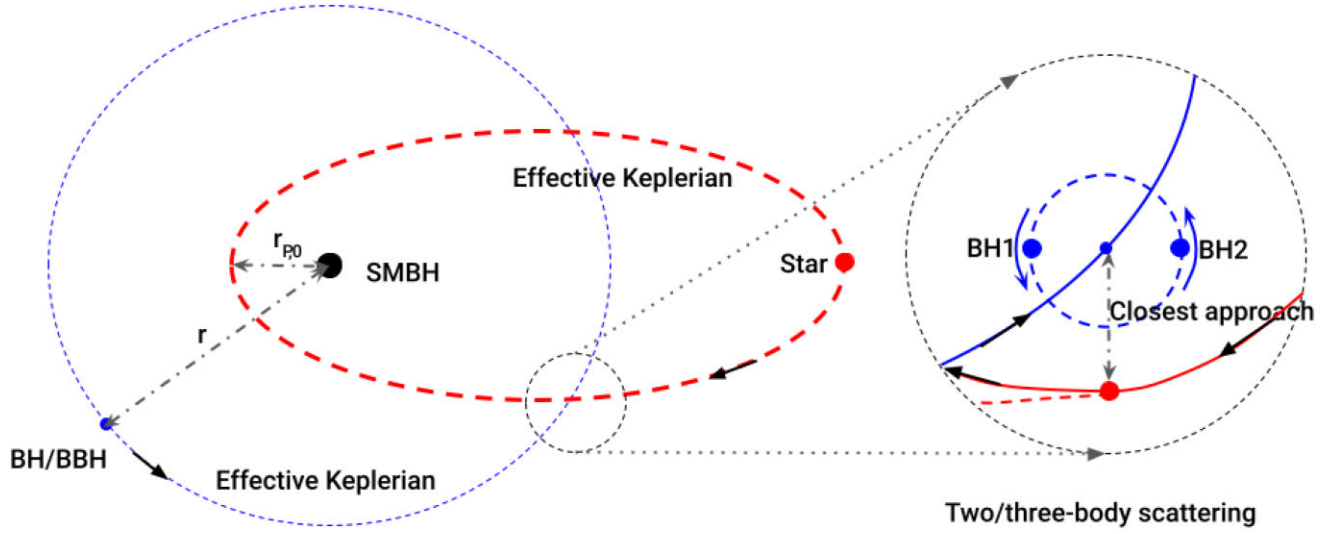

Figure 1. Schematics of the two/three-body scattering experiments in the central potential of an SMBH. *Left:* panel shows the BH/BBH in a prograde circular Keplerian orbit around the SMBH at distance r, and the star in a retrograde elliptical Keplerian orbit with the same semimajor axis r and pericentre distance $r_{P,0}$. The dashed lines represent orbits when no interaction takes place. *Right:* panel shows the two/three-body interaction between the BH/BBH and the star with a closest distance of approach between the star and BH/centre of mass of the BBH, zooming in at the scattering location, resulting in the star's orbit getting altered. The dashed thick line represents the orbit of the star if no interaction takes place, and the solid line represents the altered orbit.

(Wang et al. 2023a), akin to a rapid inspiral. As these decaying retrograde orbits shrink to the tidal disruption radius, tidal disruption events can be triggered. Once these retrograde orbits are consumed by TDEs, they cannot be efficiently replenished through the disc capture process, as the objects captured in AGN discs are in prograde orbits. Therefore, this burst of retrograde TDEs can occur only in the early stages after the AGN turns on.

The total budget of initial retrograde orbits available for TDEs, given a disc scale height $h(r)$, is

$$M_{\rm ret} \sim \int_{r_{\rm TDE}}^{r_{\rm disc,out}} {\rm d}r \int_{-1}^{-1+h^2(r)/2} d\cos I 2\pi r^2 \rho_{\rm NSC}(r)\,, \tag{17}$$

where $\rho_{\rm NSC}$ is the density of the NSC. The total mass budget for the retrograde orbiting stars is $\sim(2/3)h(r_h)M_{\rm SMBH}$ for a NSC cluster with radial density power-law index $\gamma_{\rm NSC} = 2$. The time-scale for orbital decay of the retrograde stars is

$$t_{\rm ret} \sim \frac{\Sigma_*}{\Sigma} hT = 10^{-3} \left(\frac{M_*}{1M_\odot}\right) \left(\frac{M_{\rm SMBH}}{10^8 M_\odot}\right)^{-3/2} \left(\frac{R_*}{R_\odot}\right)^{-2} \left(\frac{r}{1000\,{\rm au}}\right)^{7/2} {\rm Myr}\,. \tag{18}$$

Since $t_{\rm ret}$ is very short compared to the expected lifetime of the AGN (few Myr), we should expect an increased TDE rate very early in the AGN lifetime, before the budget for retrograde orbits has been depleted. The rate of these TDEs will be computed in Section 3.

2.3 Micro-TDEs

Apart from the normal TDEs where stars are tidally disrupted by SMBHs, within the AGN disc the high density of the stellar population makes the probability of a star being tidally disrupted by a stellar-mass black hole significant.

The 2D cross-section of a μTDE in a specific environment can be estimated by the following equation:

$$\sigma_{\mu\rm TDE} \sim \pi R_{\mu\rm TDE}^2 \left(1 + \frac{r_\sigma}{R_{\mu\rm TDE}}\right)\,, \tag{19}$$

where $R_{\mu\rm TDE} = (\frac{3M_\bullet}{M_*})^{1/3} R_*$ is the tidal radius of the star within the influence of the stellar BH of mass $M_\bullet$, and $r_\sigma \sim \frac{2G(M_\bullet+M_*)}{\sigma_{\rm env}^2}$ represents the two-body interaction radius in the environment, where gravitational forces between two objects dominate over the background potential created by other objects, with velocity dispersion denoted by $\sigma_{\rm env}$. The ratio $r_\sigma/R_{\mu\rm TDE}$ measures the strength of the gravitational focusing effect.

For objects in the NSC, the velocity dispersion scales as $\sim 2.3(M_{\rm SMBH}/M_\odot)^{1/4.38}$ km s^{-1} (Kormendy & Ho 2013), which results in $r_\sigma \sim 1000 R_\odot$ for a $10^8 M_\odot$ SMBH, $60 M_\odot$ stellar mass BH and $1 M_\odot$ main sequence star. Consequently, the gravitational focusing factor for objects in the NSC is $1 + r_\sigma/R_{\mu\rm TDE} \sim 200$.

As stars and BHs are captured by the AGN disc, they will approximately align within the same orbital plane, making the cross-section 1D, and thus the corresponding (1D) focusing factor to be proportional to $\sqrt{1 + r_\sigma/R_{\mu\rm TDE}}$. For scatterings between prograde orbits within the AGN disc, the velocity dispersion will be reduced by a factor of $\bar{b}/r$ compared to the velocity dispersion in the NSC, leading to a larger r_σ by a factor of $r/\bar{b}$. For scatterings between one prograde orbit with another retrograde orbit (retrograde scatterings), the velocity dispersion will be ~ 2 times the local Keplerian velocity; as a result, the 1D μTDE cross-section for retrograde scatterings within the AGN disc will be a few ($\sim \sqrt{1 + 200/4}$) of the 1D geometric μTDE cross-section $R_{\mu\rm TDE}$. The order of magnitude estimate provided here will be numerically quantified in Section 4.

3 SCATTERING EXPERIMENTS

Since we are focusing here on estimating the rate of TDEs and μTDEs in an AGN disc, our numerical experiments are performed in a coplanar geometry. The general set up is that of a central SMBH, a binary BH scatterer, and an incoming tertiary star, as schematically shown in Fig. 1 and further detailed in Section 3.2. To better appreciate the effect of binarity on the TDE and μTDE cross-sections, we also perform comparative experiments in which the scatterer is a single BH of mass equal to the sum of the masses of the

two BHs when in a binary (detailed in Section 3.1). Our experiments are focused on encounters with retrograde stars embedded in the disc shortly after the AGN turns on, since these are by far the most probable source of AGN TDEs.

The scattering experiments are performed using the high-precision, few-body code SPACEHUB (Wang et al. 2021b). For this work, since the mass ratio between the BHs and the SMBH is very small, and the eccentricities are large, we use the AR-chain$^+$ method of integration (Mikkola & Aarseth 1993). We ignore the post-Newtonian corrections, since the distances between the objects are large enough, and the results from the simulation show no significant differences if we include these corrections.

Note that our scattering experiments are purely gravitational and neglect hydrodynamical interactions (e.g. Lindblad resonance, corotation resonance, dynamical friction, and aerodynamic drag) on the time-scales of the scatterings. The Lindblad, corotation resonances, dynamical friction, and aerodynamical drag act on a typical time-scale that is longer than the orbital period, while the scattering time-scale is typically shorter than the orbital period. Therefore, they can be safely ignored during the scattering processes. However, we note that this assumption does not apply to resonance scatterings (i.e. multiple scatterings), where the scattering can last longer than the orbital period around the SMBH, making those dissipation processes important. For example, Li et al. (2023) and Rowan et al. (2023) have shown that dynamical friction can facilitate the formation of binary BHs in AGN discs if the two interacting objects undergo resonance scattering.

3.1 Single-single scattering

We set up coplanar scattering experiments between a BH and a star, both orbiting a SMBH, whose mass is $M_{\rm SMBH} = 10^8 {\rm M}_\odot$. This choice is motivated by the fact that most AGN masses are in the $\sim 10^7 - 10^8 M_\odot$ range.[1] We reserve a discussion of the dependence on the SMBH mass to Section 4.3. The BH has a mass $M_{\rm BH} = 60\,{\rm M}_\odot$ and lies in a circular orbit ($e_{\rm BH} = 0$) around the SMBH.

The star is initially in a highly eccentric elliptical orbit of semimajor axis equal to the orbital distance of the BH[2], and has a mass $M_* = {\rm M}_\odot$ and radius $R_* = R_\odot$. The initial pericentre distance of the star from the SMBH is increased (by decreasing the eccentricity) starting from the minimum value of $r_{P,0} = 1R_{\rm TDE}$. If the post-scattering pericentre distance of the star from the SMBH falls within this tidal disruption radius $R_{\rm TDE}$, a TDE is triggered. Similarly a μTDE is triggered if the distance between the star and the BH is smaller than $R_{\mu{\rm TDE}}$ at any time. We repeat the scattering experiments by placing the BBH across a range of disc distances: $r = [10^2, 10^5] r_g$. This range of radii is well within what expected from detailed modelling of AGN discs (Sirko & Goodman 2003; Thompson, Quataert & Murray 2005).

3.2 Binary-single scattering

For binary-single scattering, we take the same setup and replace a single BH with a binary BH with equal total mass ($60{\rm M}_\odot$). The BBH is in a perfectly circular ($e_{\rm BBH} = 0$) prograde orbit. We explore a range of BBH radial locations from $r = 10^2 r_g$ to $10^5 r_g$ and three different sized binaries $a_{\rm BBH} = [0.01, 0.1, 1]R_{\rm H}$ where

$$R_{\rm H} = \left(\frac{M_{\rm BBH} + M_*}{3M_{\rm SMBH}}\right)^{1/3} r \tag{20}$$

is the mutual Hill radius of the BBH and the star.

Similarly, the initial semimajor axis of the orbit of the star was set up to be the same as the orbit of the BBH around the SMBH. The initial pericentre distance of the star from the SMBH is varied from $r_{P,0} = 1R_{\rm TDE}$ to 5 $R_{\rm TDE}$, resulting in a highly eccentric retrograde orbit. For each set of parameters, one million scattering experiments were performed to obtain statistically significant results.

4 RESULTS

4.1 Scattering outcomes via phase-space diagrams

The scattering experiments were performed by fixing the distance r between the SMBH and the BHs, and the initial pericentre distance of the star $r_{P,0}$. This effectively fixes the initial eccentricity of the orbit, since $e = 1 - r_{P,0}/r$ for an elliptical orbit. For single-single scattering, the only variable parameter then is the closest distance of approach between the star and BH, or equivalently the impact parameter.

For binary-single scattering, the initial phase ϕ of the BBH introduces a new variable to the problem (in addition to the distance of closest approach between the star and the BBH). We now vary the distance of closest approach to the centre of mass of the binary (rather than the distance to a single BH as in the single-single scatterings), and ϕ, to explore areas of parameter space where TDEs or μTDEs could be triggered.

Fig. 2 shows our results for the smallest BBH size $a_{\rm BBH} = 0.01R_{\rm H}$. The left column shows our results for the distance $r = 10^3 r_g$, the right column shows the same for $r = 10^4 r_g$. The colourbar indicates the ratio of the final pericentre distance to the initial pericentre distance of the star from the SMBH. At the bottom of each plot, we have indicated the percentage of scenarios that result in TDEs, up to the given maximum closest approach, which is equal to $10a_{\rm BBH}$ in the experiments. The top row shows cases with initial pericentre distance $r_{P,0} = 1R_{\rm TDE}$, and the bottom row shows cases with $r_{P,0} = 2R_{\rm TDE}$.

In Fig. 2, we can see that as we increase $r_{P,0}$ (from top to bottom), the parameter space resulting in TDEs decreases sharply. This is not surprising since the initial orbit of the star has a pericentre that is farther from the SMBH, so the interaction with the BBH is rarely strong enough to scatter the star to within the tidal disruption radius of the SMBH. Indeed, when we further increase the initial pericentre distance to $r_{P,0} = 5R_{\rm TDE}$, no TDEs are observed, and thus the results have not been included.

Similarly, Fig. 3 shows our results for the BBH size $a_{\rm BBH} = 0.1R_{\rm H}$, while the rest of the parameters are the same as in Fig. 2. We see a similar trend with $r_{P,0}$ regardless of the size of the binary, though this larger binary generates fewer overall TDEs. However, when the size of the BBH is smaller, the BBH has steeper gravitational potential and thus scatterings can be stronger. This can be seen by comparing the results in Figs 2 and 3. Comparing the same set of initial parameters in the two figures, the fraction of scenarios resulting in TDEs, i.e. the star getting scattered closer to the SMBH, increases for smaller $a_{\rm BBH}$. The fraction of scenarios where the star gets scattered farther away from the SMBH also increases, which is evident from the maximum value of the colourbar.

A third scenario was explored, where the BBH size $a_{\rm BBH} = 1.0R_{\rm H}$, but it has not been included in the results since this BBH is easily

[1] http://www.astro.gsu.edu/AGNmass/

[2] For retrograde encounters, which, as we will show, are dominated by highly eccentric orbits, the bulk of the TDE events comes from the relatively more nearby stars to the scatterer, which are captured by this initial condition.

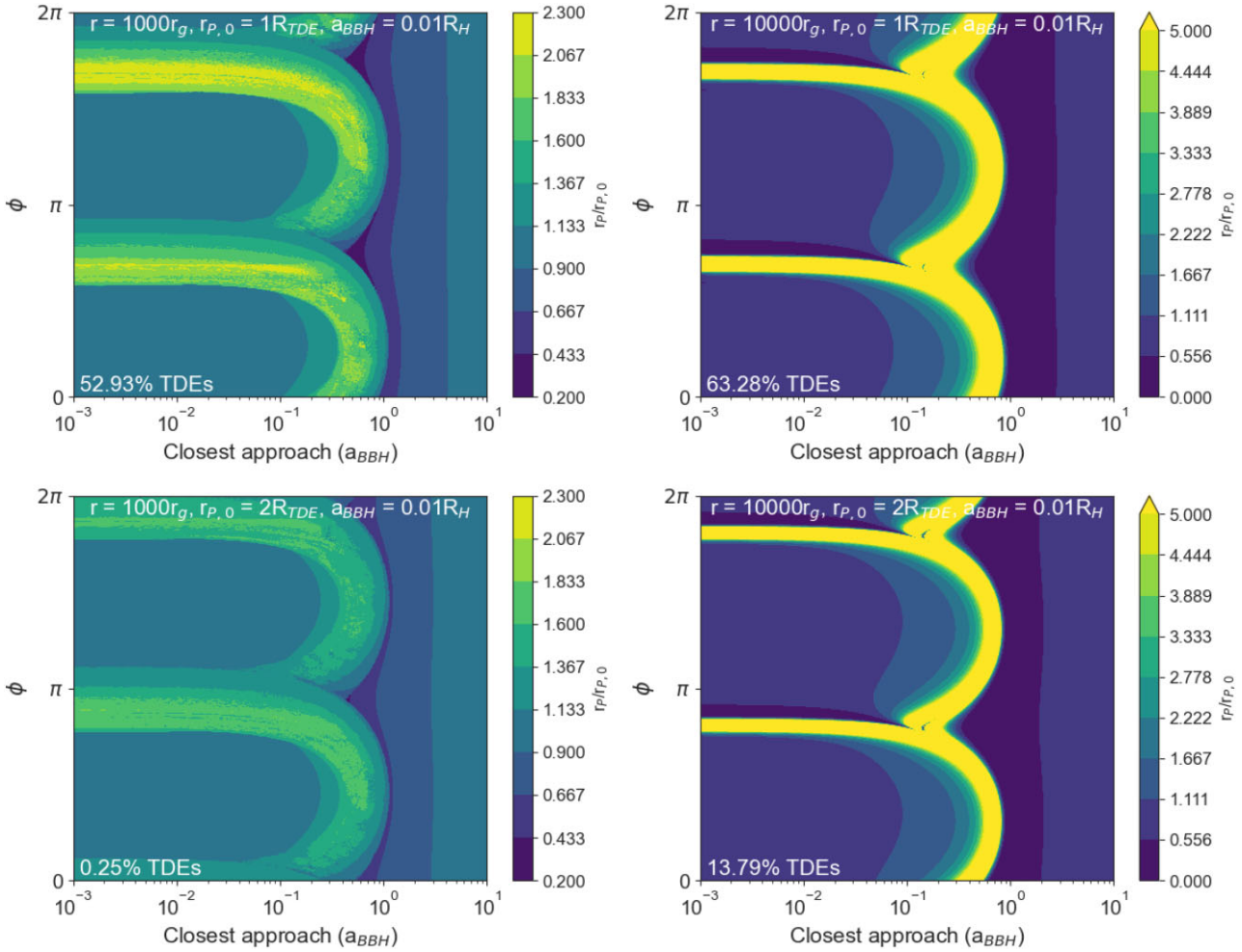

Figure 2. Phase space diagrams illustrating the results of the scattering experiments between a star and a BBH of size $a_{\rm BBH} = 0.01R_{\rm H}$. The colourbar indicates the ratio between the final pericentre distance and the initial pericentre distance of the star from the SMBH, as a function of the closest approach distance between the star and the centre of mass of the BBH in units of the BBH size and the initial phase ϕ of the BBH. Above each figure is listed the scattering location r, the initial pericentre distance of the star from the SMBH $r_{P,0}$, and the size of the BBH $a_{\rm BBH}$. At the bottom of each figure is listed the percentage of the phase space in which a TDE is observed.

disrupted by the incoming star, and does not produce any significant number of TDEs.

All the scenarios shown in Figs 2 and 3 have stars with highly eccentric pre-scattering orbits ($e \approx 1$), going almost directly towards the SMBH, with difference in eccentricities of the order of 10^{-2}. However, the number of TDEs sharply drops going from the top row to the bottom row as the initial eccentricity of the star is decreased minutely. This shows that TDEs resulting from scattering dynamics require highly initial eccentricity, almost radial initial orbits. Our results show that the change in the orbit of the star as a result of scattering is not significant enough in most cases, as the ratio of the final and the initial pericentre distance is of the order of $\sim 1 \sim 10^0$ in most scenarios.

We now compare our results from the binary-single scattering to those from the single-single scattering. Since our interest is in the production of TDEs, we restrict ourselves to the parameter space for which scatterings in the single BH case lead to the star being scattered towards the SMBH rather than away from it. This gives a conservative cross-section within a factor of $\lesssim 2$ for the BBH scatterer, and no difference for the single BH one. In Fig. 4, we show the ratio of the final pericentre distance and the initial pericentre distance of the star from the SMBH. The black solid line shows our results for a single $60{\rm M}_\odot$ BH scattering a star at a distance $r = 10^3 r_g$ and initial pericentre distance $r_{P,0} = 1R_{\rm TDE}$, corresponding to an initial eccentricity $e = 1 - r_{P,0}/r \approx 0.99$. We compare this with our results for a $30{\rm M}_\odot$–$30{\rm M}_\odot$ BBH scattering a star with the same initial eccentricity as the single BH scenario. For the binary scenario, we adopted two different binary sizes, $0.01R_{\rm H}$ and $0.1R_{\rm H}$. The left plot shows results for the BBH size $a_{\rm BBH} = 0.01R_{\rm H}$, and the right plot shows results for $a_{\rm BBH} = 0.1R_{\rm H}$, and vertical black dashed line in each plot indicates the size of the BBH. In each plot, the blue dots show results from BBH scatterings with the same initial parameters as those in the single BH scattering experiment: $r = 10^3 r_g$, $r_{P,0} = 1R_{\rm TDE}$, while the orange dots show results from BBH scatterings with: $r = 10^4 r_g$, $r_{P,0} = 10R_{\rm TDE}$, thus effectively keeping the initial eccentricity of the star fixed.

Our results show that for interactions where the impact parameter is larger than the size of the BBH, the scattering is almost identical to that from a single BH. But for impact parameters smaller than this, we see two different branches of the post-scattered orbits. One branch is that of stars that get scattered towards the SMBH, similar to being scattered by a single BH, but with a wide range of final orbits due to

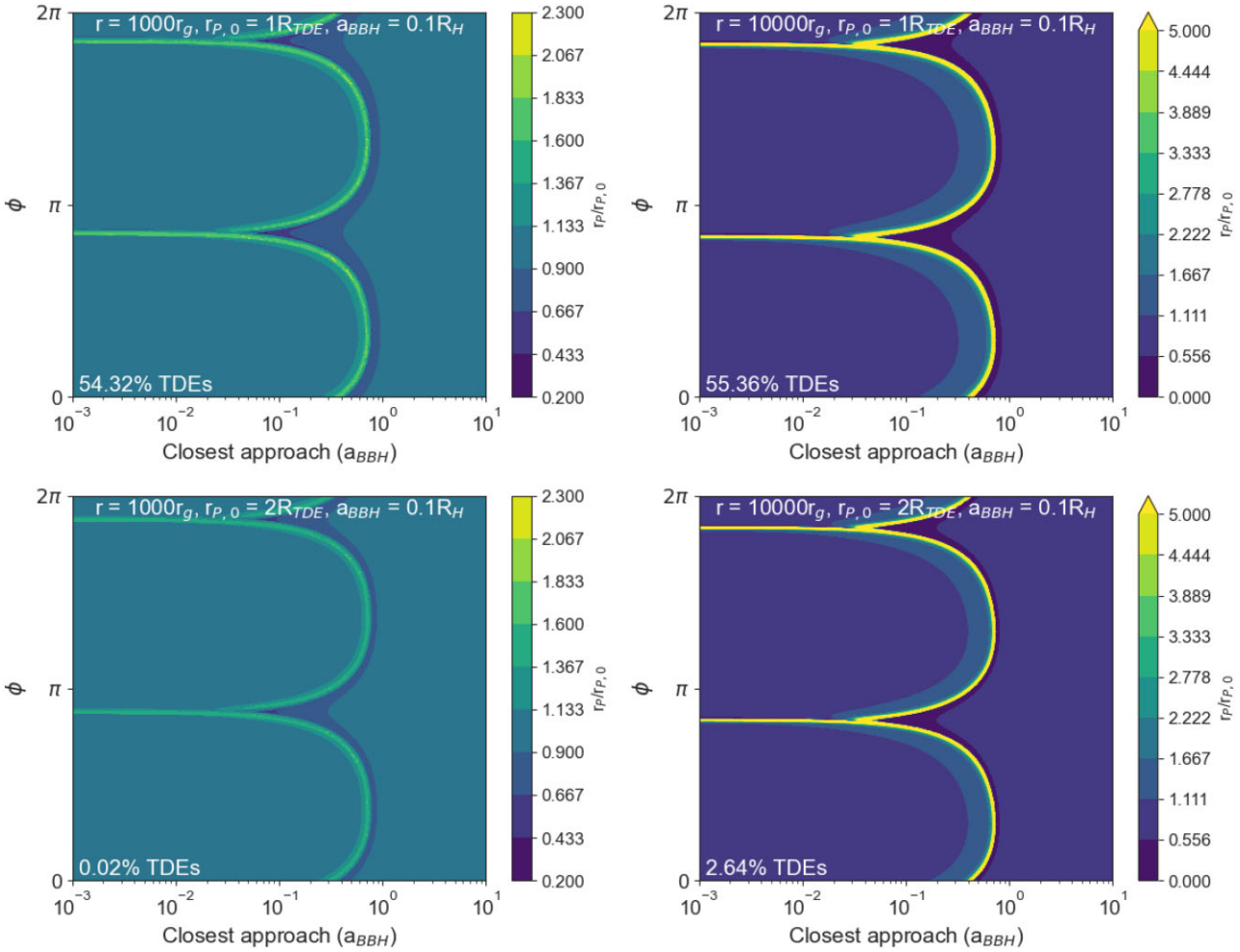

Figure 3. Same as Fig. 2 but with BBH of size $a_{\rm BBH} = 0.1R_{\rm H}$.

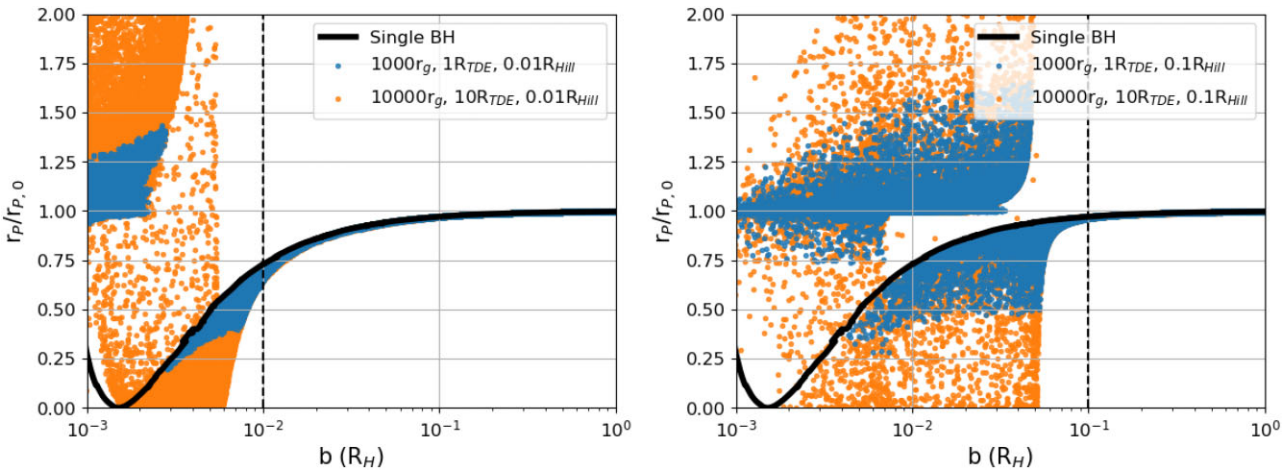

Figure 4. Ratio of the final pericentre distance of star from SMBH to the initial pericentre distance as a function of the impact parameter b. The solid line shows results for a single BH scatterer at $r = 10^3 r_g$ and the initial pericentre distance of the star $r_{P,0} = 1R_{\rm TDE}$. The left panel shows the results for BBH of size $a_{\rm BBH} = 0.01R_{\rm H}$, while the right panel shows the same for BBH of size $a_{\rm BBH} = 0.1R_{\rm H}$, the dashed vertical lines mark the size of the BBH. The two sets of parameters shown in both the figures are: $[r = 10^3 r_g,\ r_{P,0} = 1R_{\rm TDE}]$ and $[r = 10^4 r_g,\ r_{P,0} = 10R_{\rm TDE}]$.

the different phases ϕ of the BBH. The other branch is that of stars that get scattered away from the SMBH, which are not present in the single BH scattering. When the star interacts with the BBH with an impact parameter much smaller than the size of the BBH, the star goes through the BBH, and can get pulled in opposite directions from the individual BHs, one pulling it closer to the SMBH and the other pulling it away. The second branch results from scenarios where the star is closer to the BH pulling the star away from the SMBH, and the

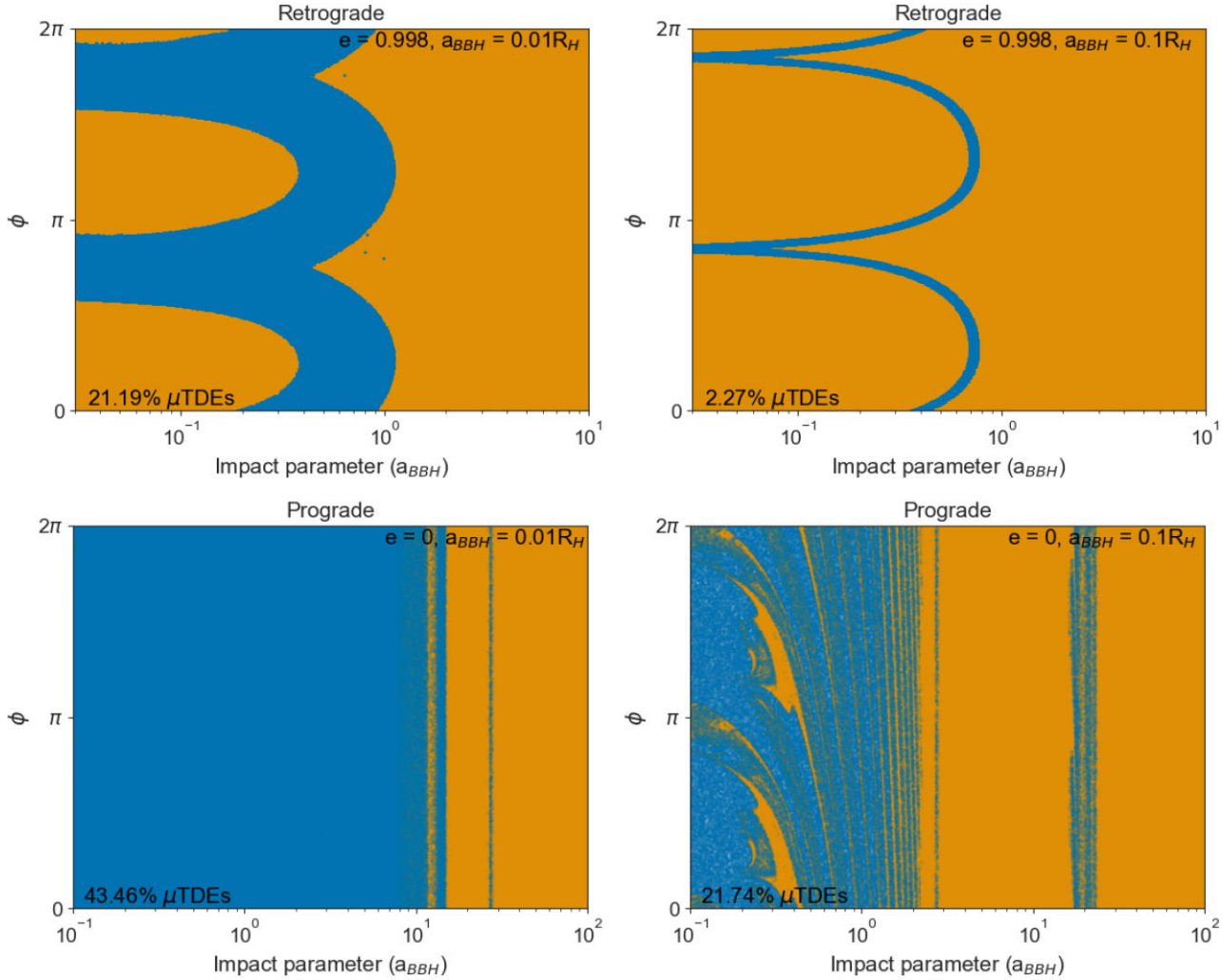

Figure 5. Phase diagrams illustrating the regions of initial binary phases and impact parameters for which scatterings lead to a μTDE (blue dots) rather than to a simple scattering (orange dots). The BBH scatterer is placed at a radial distance $r = 10^3 r_g$. Stars in prograde orbital motion are assumed to have an initial eccentricity $e = 0$, while stars in retrograde motion come in nearly radial orbits. The cases shown here have initial eccentricity $e = 0.998$ as a representative example. Left and right panels illustrate how the scattering outcome changes with the size of the binary. The numbers quoted in the panels indicate the total fraction of μTDEs integrated over all phases and impact parameters shown.

net effect is a post-scattered orbit with a larger pericentre distance from the SMBH.

Next, with a similar analysis to that of the standard TDE scenario, we use our scattering experiments to generate phase-space diagrams in order to identify the regions in the parameter space leading to μTDEs. In Fig. 5, the left column shows the phase-space leading to μTDEs (blue dots) for the BBH size $a_{\rm BBH} = 0.01R_{\rm H}$, while the right column shows the same for $a_{\rm BBH} = 0.1R_{\rm H}$. Unlike standard TDEs, which are much more likely to occur as a result of the nearly radial orbits of retrograde stars, μTDEs can sizeably result from a wide range of eccentricities. More importantly, unlike standard TDEs in AGN discs, where prograde scattering barely contributes, μTDEs occur frequently in both prograde and retrograde scatterings. Therefore, we explore both prograde and retrograde scatterings. We display the results at the representative scattering location $r = 10^3 r_g$.

We assume an initially circular orbit for stars in prograde orbits (initial $e = 0$), while for retrograde orbits we consider a typical case of a highly eccentric orbit, with initial $e = 0.998$. The top panels of Fig. 5 display our scattering experiment results for retrograde star orbits, while in the bottom panels we show our results for prograde star orbits. For each case, the left and right panels illustrate the dependence of the scattering experiments on the binary size. At the bottom of each plot, we indicate the total fraction of events (i.e. integrated over the full phase space shown) that results in μTDEs.

For prograde orbits, the relative velocity between the BBH and the star is small. This leads to a larger gravitational focusing factor as described in Section 2.3. As a result, μTDEs appear in a larger region of the parameter space.

In the case of retrograde orbits, the star is in a highly eccentric, nearly radial path towards the SMBH, and the relative velocity between the BBH and the star is large. As a result, the gravitational focusing effect is much weaker than the prograde scatterings. Due to this reason, when the impact parameter is small, the star can easily pass through the BBH without encountering either of the component BHs.

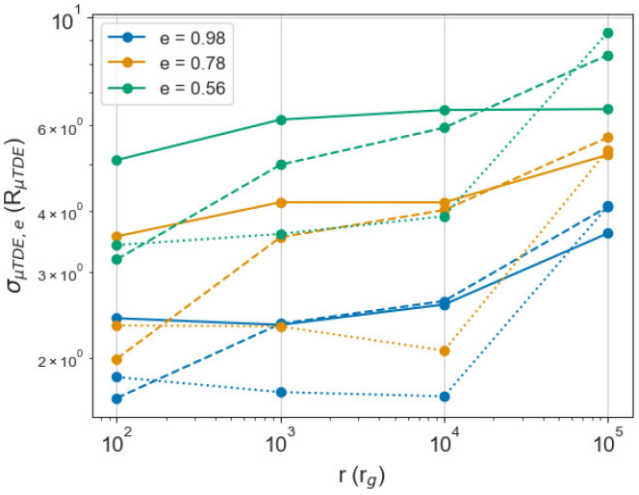

Figure 6. μTDE (disruption by the stellar mass BH) cross-section as a function of the distance r from the SMBH for different initial eccentricities of the disrupted star (incoming in a retrograde orbit). The solid line shows results for a BBH of size $a_{\rm BBH} = 0.1R_{\rm H}$, the dashed line shows results for a BBH of size $a_{\rm BBH} = 0.01R_{\rm H}$, and the dotted line shows results for a single BH.

4.2 Cross-sections

The cross-section of a star undergoing a TDEs is given by

$$\sigma_{\rm TDE} = \int_{\Sigma L_{\rm TDE}} {\rm d}b, \tag{21}$$

where the integration is performed over the impact parameter b, identifying the regions $\Sigma L_{\rm TDE}$ in the parameter space where TDEs are observed. The impact parameter is expressed in units of the Hill radius, $R_{\rm H}$, thus the cross-section is calculated in units of $R_{\rm H}$ for standard TDEs, while for μTDEs the cross-section is calculated in units of $R_{\mu TDE}$ corresponding to a 60 $M_\odot$ BH (note the units of length – rather than length square, since we are in a coplanar geometry). This integration needs to be performed over the entire range of initial pericentre distances of the orbit of the star, or equivalently over the entire range of initial eccentricities.

From above, the probability distribution of the orbital eccentricity of stars will depend on whether they are in prograde or retrograde orbits. The former, after a possibly transient period, will eventually settle in circular orbits, and (relatively) slowly migrate through the disc due to gas torques, subject to occasional perturbations from in-disc binary-single scattering. The latter (stars on retrograde orbits) will develop a very high eccentricity. For these stars in retrograde orbits it can be assumed that the initial orbital angular momentum has a uniform probability distribution function, such that $p(L) =$ constant (see Appendix A for a justification). Then the eccentricity probability distribution $p(e)$ readily follows from

$$p(e) = p(L)|{\rm d}L/{\rm d}e| \propto \frac{e}{\sqrt{1-e^2}}, \tag{22}$$

where $p(e)$ is normalized to unity using $\int_0^1 dep(e) = 1$. The cross-section is computed by drawing random values of the eccentricity from this distribution.

For the computation of the cross-section of standard TDEs onto the SMBH, we only focus on cases where the TDEs are induced due to the scattering from the BH/BBH. This is determined by scenarios where the pre-scattering pericentre distance of the star is larger than the SMBH tidal disruption radius, but post-scattering it becomes smaller than it, thus leading to a scattering-induced TDE. We compute this cross-section for three different sizes of the scattering BBH: $a_{\rm BBH} = 0.1R_{\rm H}$, $a_{\rm BBH} = 0.01R_{\rm H}$, and $a_{\rm BBH} = 0$, which effectively corresponds to the case of a single BH of total mass equal to the sum of the two BHs in the binary. Our numerical experiments show that this cross-section is largely independent of the size of BBH and its distance from the SMBH, and is on the order of $\sigma_{\rm TDE} \sim 1 \times 10^{-3} R_{\rm H}$. So, larger mass BBH ($R_{\rm H} \propto M_{\rm BBH}^{1/3}$) at larger radial disc distance ($R_{\rm H} \propto r$) will be more efficient TDE generators per scattering encounter (although more frequent encounters occur at small r).

For the computation of the cross-section of μTDEs, we assume circular orbits for stars in prograde orbits, and the same probability in equation (22) for stars in retrograde orbits. In order to gain physical insight into the range of orbital parameters more likely to yield μTDEs, we begin by showing the cross-sections at fixed values of the initial eccentricity e, for each distance r of the scatterer from the SMBH.

Unlike standard TDEs, which are largely favoured by radial orbits, μTDEs are more easily favoured by lower eccentricities. For high eccentricities, the star has a near straight-line path. Due to the large relative velocity between the star and the BBH, the time spent by the star in close vicinity of the BBH is small. As the eccentricity is lowered, the star takes a more curved path. The relative velocity between the star and the BBH is significantly reduced; as a result, the star spends more time close to the BBH, leading to a higher probability of being disrupted by either of the component BHs. This effect is even stronger when the BBH size is large since a larger BBH allows the star larger window of time to encounter a component BH. If the BBH is replaced by a single BH, this window of time is smaller and the probability of a μTDE is smaller. This is illustrated by Fig. 6, where we show our results for the μTDE cross-sections for three different initial eccentricities of the star (incoming in a retrograde orbit), and for two different sized BBH and single BH scattering.

In terms of the trend with distance r of the BH/BBH from the SMBH we note that, generally, the rate of μTDEs stays nearly constant in inner regions and increases as $r^{1/2}$ in the outer regions, as also found in the two-body case by Wang et al. (2023b). This is due to the fact that, in the outer region, the orbital velocity difference between the star and the BH/BBH around the SMBH is significantly smaller than in the inner region. Thus, the gravitational focusing effect in the outer region is stronger. Since the star will be disrupted at the fixed radius $R_{\mu\rm TDE}$, a stronger focusing effect in the outer region leads to a larger cross-section of the μTDE.

The net cross-section, weighted by the probability distribution $p(e)$ at each scattering location r, is displayed in Fig. 7 for a range of binary sizes. Following the trend in Fig. 6, the magnitude of the net cross-section shows a small dependence on the distance r; also, the larger BBH has a slightly larger cross-section.

Last, Fig. 8 shows the scattering experiment results for the cross-section of μTDEs for stars in prograde, circular orbits. Due to the smaller relative velocities, the gravitational focusing effect is especially strong in prograde scatterings, which contribute most of the μTDEs in AGN discs. This effect is even stronger in the outer regions of the disc since the relative velocity between the star and the BBH decreases with increasing distance r, and thus the cross-section displays a steep increase with r.

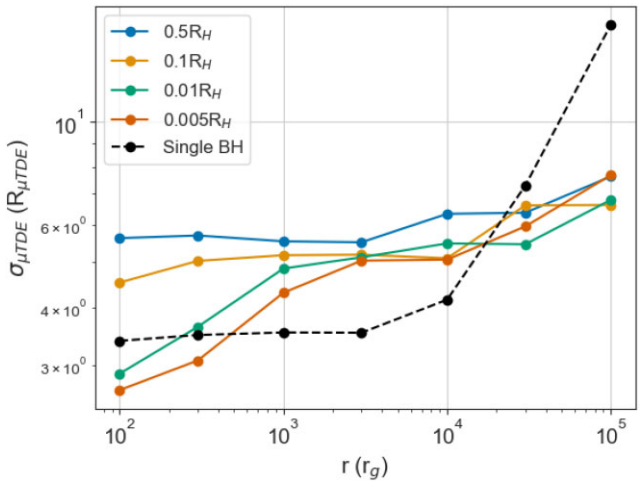

Figure 7. Cross-sections of μTDEs for retrograde stars as a function of the distance r of the sBH/BBH location from the SMBH. Initial eccentricities are drawn from a uniform probability in angular momentum for the incoming star.

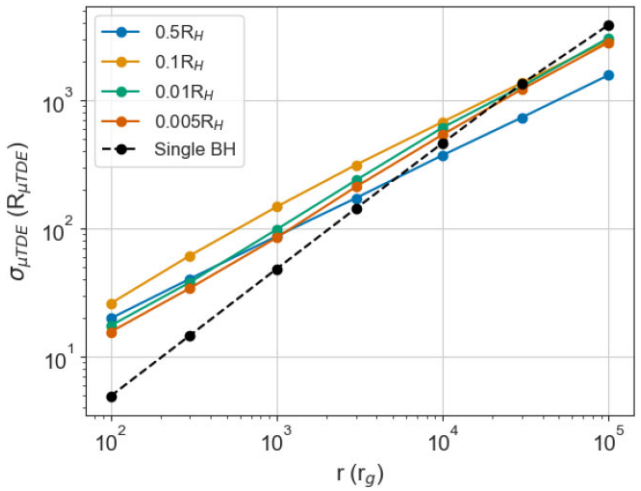

Figure 8. Cross-section of μTDEs for stars in prograde, circular orbits as functions of the distance r of the sBH/BBH location from the SMBH.

4.3 From cross-sections to event rates

We begin by calculating the event rate per system (per BH for single scattering and per BBH for binary scattering) by using:

$$\gamma = 2H\sigma_{\rm TDE} n_* v, \tag{23}$$

where n_* represents the number density of stars within the disc, and v is the relative velocity between the stars and the BH/BBH centre of mass. Since $H/r \ll 1$, the scatterings are almost identical within the scale height H of the disc at a given r. We obtain the normally defined cross-section (in unit of area) by multiplying $\sigma_{\rm TDE}$ by the thickness of the disc $2H$, as given by equation (11).

Given the poorly constrained population of stars in AGN discs, we use the number density n of stars in the NSC to provide a rough approximation to the number density n_* of stars in the AGN discs.

The number density n of stars in the NSC follows a power-law distribution characterized by the index $\gamma_{\rm NSC}$, as given by (Merritt & Poon 2004; Merritt 2013):

$$n = \frac{3-\gamma_{\rm NSC}}{2\pi}\frac{M_{\rm SMBH}}{m} r_h^{-3}\left(\frac{r}{r_h}\right)^{-\gamma_{\rm NSC}}. \tag{24}$$

Here, m represents the average mass of a star in the NSC, and r_h is the gravitational influence radius of the SMBH.

For the relative velocity between the star and the BH/BBH (v), in retrograde scatterings (i.e. the stars move in the opposite direction to the BH/BBH), we use $2v_{\rm k}$, where $v_{\rm k}$ is the local Keplerian velocity. For prograde scatterings, we use the shear velocity difference $\frac{dv_{\rm k}}{dr}\langle\Delta r\rangle$, where $\langle\Delta r\rangle \sim (1/n)^{1/3}$ is the average distance between objects in the disc, which can be obtained from equation (24).

To obtain the global rate of the scattering induced TDE/μTDE, we integrate $\gamma_{\rm TDE}$ over the disc volume

$$\Gamma \sim \int n_\bullet \gamma {\rm d}V \sim \int_0^{r_{\rm max}} n_\bullet \gamma 2\pi r 2H(r){\rm d}r\,, \tag{25}$$

where $n_\bullet$ is the number density of BH/BBH in the AGN discs, and $r_{\rm max}$ is the minimum between r_h and $10^5 r_g$, which is the maximum radius of our scattering experiments, set as a conservative limit given the uncertain exact value of the disc outer radius. For simplicity (and lack of detailed estimates in the literature), we assume that stars and BHs/BBHs follow the same density profile of the stars. We note however that this is most likely not strictly the case, since, due to mass segregation, BHs tend to migrate towards the inner cluster regions, where their abundance compared to that of the stars thus becomes relatively higher compared to the outer regions (Generozov et al. 2018). To keep transparent the dependence of our rates Γ on $n_\bullet$, we define the BH-to-star ratio $f_\bullet = n_\bullet/n$, and express the rates in terms of this quantity. We will use as a reference in the rescaling the value $f_\bullet = 0.01$, comparable to the fraction found in the inner NSC regions by Generozov et al. (2018).

For standard TDEs by the SMBH, which we studied for retrograde stars, we estimate about $(6\times10^{-5}$–$5\times10^{-2})(f_\bullet/0.01)$ scattering induced TDEs per year, largely independent of whether the scatterer is a single BH or a BBH, and also largely independent of the size of the BBH. The range of rates corresponds to the interval $\gamma_{\rm NSC} \sim 1$–2, respectively. We note (not surprisingly) that this scattering-induced TDE rate, while being relatively high during this AGN 'turn-on' phase, when highly eccentric stars are produced, it is however subdominant with respect to the main TDE flow due to stars on nearly radial orbits which migrate towards the SMBH without help from scattering, and which has been discussed in detail in previous works (McKernan et al. 2022b; Wang et al. 2023b).

For the rate of μTDEs and encounters with retrograde stars, we estimate about $(2\times10^{-5}$–$3\times10^{-2})(f_\bullet/0.01)$ events per year if the scatterer is a binary, while for single BH scattering the rate increases to $(5\times10^{-5}$–$4\times10^{-2})(f_\bullet/0.01)$ per year. For prograde stars, we estimate $(1\times10^{-4}$–$4\times10^{-2})(f_\bullet/0.01)\,\mu$TDEs events per year again largely independent of whether the scatterer is a single BH or a BBH. Likewise above, the interval for the rates corresponds to the range $\gamma_{\rm NSC} \sim 1$–2.

The reported rate upper limits mentioned above apply to a $10^8 M_\odot$ SMBH, which is a representative SMBH for AGNs. For SMBHs of other masses, the rates can be obtained using the following scalings:

$$\dot{M} \propto M_{\rm SMBH} \tag{26}$$

$$H \propto \Omega_d^{-1/3} \propto M_{\rm SMBH}^{-1/6} \tag{27}$$

$$r_h \propto M_{\rm SMBH}\sigma_{\rm NSC}^{-2} \propto M_{\rm SMBH}^{0.54} \tag{28}$$

$$n \propto (3-\gamma_{\rm NSC}) M_{\rm SMBH}^{0.54(\gamma_{\rm NSC}-3)+1} \tag{29}$$

$$v_{\rm ret} \propto v_k \propto M_{\rm SMBH}^{1/2} \tag{30}$$

$$v_{\rm pro} \propto v_k n^{-1/3} \propto M_{\rm SMBH}^{1/6-0.18(\gamma_{\rm NSC}-3)} \tag{31}$$

$$\sigma_{\rm TDE} \propto R_{\rm TDE} \propto M_{\rm SMBH}^{1/3} \tag{32}$$

$$\sigma_{\mu\rm TDE} \propto M_{\rm SMBH}^{0}\,. \tag{33}$$

For $\sigma_{\rm NSC}$, we use the M–σ relation $\sigma_{\rm NSC} \propto M_{\rm SMBH}^{1/4.38}$(Kormendy & Ho 2013).

For prograde scatterings (denoted (p,TDE)), the rates scale according to the following relationships (using $r_{\rm max} = r_h$ for generality):

$$\gamma_{\rm p,TDE} \propto M_{\rm SMBH}^{0.36(\gamma_{\rm NSC}-3)+4/3} \tag{34}$$

$$\gamma_{\rm p,\mu TDE} \propto M_{\rm SMBH}^{0.36(\gamma_{\rm NSC}-3)+1} \tag{35}$$

$$\Gamma_{\rm p,TDE} \propto M_{\rm SMBH}^{1.9} \tag{36}$$

$$\Gamma_{\rm p,\mu TDE} \propto M_{\rm SMBH}^{1.02}\,. \tag{37}$$

For retrograde scatterings [denoted (r,TDE)], the rates scale as follows:

$$\gamma_{\rm r,TDE} \propto M_{\rm SMBH}^{0.54(\gamma_{\rm NSC}-3)+5/3} \tag{38}$$

$$\gamma_{\rm r,\mu TDE} \propto M_{\rm SMBH}^{0.54(\gamma_{\rm NSC}-3)+4/3} \tag{39}$$

$$\Gamma_{\rm r,TDE} \propto M_{\rm SMBH}^{2.23} \tag{40}$$

$$\Gamma_{\rm r,\mu TDE} \propto M_{\rm SMBH}^{1.36}\,. \tag{41}$$

These scalings provide a framework for estimating the rates of TDEs and μTDEs for SMBHs of various masses based on the dynamics within the AGN discs.

5 DISCUSSION

Using idealized three body scattering experiments, we have explored a wide range of scenarios that can generate an AGN TDE around the central SMBH, or an AGN μTDE from stellar-mass BHs embedded in an AGN disc. We focused on the scattering of retrogade orbiting stars by BH binaries (BBHs), given their large geometric cross-sections, and the likelihood of BBHs in an AGN disc. We investigated a range of BBH sizes and BBH locations in the disc.

Standard loss-cone filling by dynamical encounters is inefficient in AGN. However, stars on retrograde orbits should be about half the initial stellar population early ($\leq$0.1 Myr) in the AGN lifetime. Fully embedded retrograde stars should rapidly acquire a very high eccentricity and can either end up directly disrupted by the SMBH, or be scattered into the AGN loss-cone (McKernan et al. 2022b). Thus, AGN TDEs should overwhelmingly arise early in an AGN lifetime before the retrograde orbiters disappear. We find TDE rates of $\sim (6\times10^{-5} - 5\times10^{-2})(f_\bullet/0.01)\,{\rm AGN}^{-1}{\rm yr}^{-1}$ which spans comparable to or significantly higher than the 'naked' TDE rate O(10^{-4} galaxy^{-1}yr^{-1}). The magnitude of the AGN TDE rate is determined by a combination of the slope of the NSC density profile and the outer disc radius, with very little dependence on the BBH size. AGN TDEs from retrograde orbiters may display significantly higher luminosities than naked TDEs, or prograde TDEs, with optical/UV luminosity up to $\sim10^{44}$ erg s^{-1} and should significantly heat the inner AGN disc (McKernan et al. 2022b), which may be detectable in large AGN surveys. An additional source of AGN TDEs may be due to stars on prograde orbits, via multiple scatterings, which is deferred to future work.

The dynamical conditions leading to μTDEs are both qualitatively and quantitatively different than for standard TDEs. In this case, lower eccentricities are generally favoured, and hence there can be contributions also from prograde orbiters. We find μTDEs rates of $\sim(1\times10^{-4} - 4\times10^{-2})(f_\bullet/0.01){\rm AGN}^{-1}$ yr^{-1} (prograde), and $\sim(2\times10^{-5} - 3\times10^{-2})(f_\bullet/0.01)\,{\rm AGN}^{-1}$ yr^{-1} (retrograde). While AGN TDEs should be dominated by stars on retrograde orbits and appear mostly early in the AGN lifetime, μTDEs from stars on prograde orbits are present throughout the AGN lifetime, thus providing a great probe to study the population of embedded objects over the entire AGN cycle. Also importantly, while retrograde encounters tend to be hyperbolic and hence not expected to lead to flaring since the debris get unbound (see e.g. Hayasaki et al. 2018), prograde encounters are eccentric, and the debris will thus remain bound, hence allowing the needed rapid accretion to power TDE flares. Recent work suggests that debris, particularly from retrograde TDEs, can be fully mixed into dense AGN disc, and the perturbation of the inner disc by the TDE will generate a state-change, likely accounting for some observations of changing look AGN (Ryu et al. 2024b).

The duration, light curves, and spectra of TDEs and μTDEs are expected to differ in multiple ways. The lower BH mass in μTDEs results in accretion rates which can exceed the Eddington threshold by up to a factor of 10^5 or more (Metzger & Stone 2016; Kremer et al. 2019, 2022; Lopez et al. 2019; Wang et al. 2021a). The combination of high accretion rates and low BH masses in μTDEs results in hotter discs compared to those of standard TDEs (Wang et al. 2021a), leading to a high X-ray luminosity. Most importantly, the hyper-Eddington accretion rates are likely to create conditions conducive to the launch of relativistic outflows which may then dissipate yielding significant γ-ray and X-ray emission (Murase et al. 2016). Such emission, longer but weaker than that of the standard GRBs, may rather resemble that of the ultralong GRBs (Perets et al. 2016).

Finally, detection from AGN discs eventually requires the radiation to pass through the dense disc material on its way to the observer. Depending on the AGN disc mass and scatterer distance from the SMBH, the radiation can emerge unaltered, marginally diffused, or highly diffused (Perna, Lazzati & Cantiello 2021a; Zhu et al. 2021; Wang, Lazzati & Perna 2022), resulting in increasingly dimmer but longer lived transients. Future searches for signatures of AGN TDEs and μTDEs in large samples of AGN will help constrain the dynamics of embedded populations in AGN discs over typical AGN lifetimes.

ACKNOWLEDGEMENTS

CP and RP acknowledge support by NSF award AST-2006839. BM & KESF are supported by NSF AST-2206096 and NSF AST-1831415 and Simons Foundation Grant 533845 as well as Simons Foundation sabbatical support. The Flatiron Institute is supported by the Simons Foundation. YW is supported by the Nevada Center for Astrophysics. We thank the anonymous referee for an exceptionally constructive and thoughtful report which helped to considerably improve the paper.

DATA AVAILABILITY

Any data used in this analysis are available on reasonable request from the first author (CP).

REFERENCES

Abbott R. et al., 2020a, Phys. Rev. Lett., 125, 101102
Abbott B. P. et al., 2020b, ApJ, 892, L3
Artymowicz P., Lin D. N. C., Wampler E. J., 1993, ApJ, 409, 592
Arzamasskiy L., Zhu Z., Stone J. M., 2018, MNRAS, 475, 3201
Bartos I., Kocsis B., Haiman Z., Márka S., 2017, ApJ, 835, 165
Bellovary J. M., Mac Low M.-M., McKernan B., Ford K. E. S., 2016, ApJ, 819, L17
Binney J., Tremaine S., 1987, Galactic Dynamics. Princeton Univ. Press, Princeton
Blanchard P. K. et al., 2017, ApJ, 843, 106
Callister T. A., Haster C.-J., Ng K. K. Y., Vitale S., Farr W. M., 2021, ApJ, 922, L5
Cannizzaro G. et al., 2020, MNRAS, 493, 477
Cannizzaro G., Levan A. J., van Velzen S., Brown G., 2022, MNRAS, 516, 529
Cantiello M., Jermyn A. S., Lin D. N. C., 2021, ApJ, 910, 94
Chandrasekhar S., 1942, Principles of Stellar Dynamics. Dover Publications, New York
Dexter J., Begelman M. C., 2018, MNRAS, 483, L17
Dittmann A. J., Miller M. C., 2020, MNRAS, 493, 3732
Dittmann A. J., Cantiello M., Jermyn A. S., 2021, ApJ, 916, 48
Du P., Egaña-Ugrinovic D., Essig R., Fragione G., Perna R., 2022, Nat. Commun., 13, 4626
Elitzur M., 2012, ApJ, 747, L33
Elitzur M., Ho L. C., Trump J. R., 2014, MNRAS, 438, 3340
Eracleous M., Livio M., Halpern J. P., Storchi-Bergmann T., 1995, ApJ, 438, 610
Fabj G., Nasim S. S., Caban F., Ford K. E. S., McKernan B., Bellovary J. M., 2020, MNRAS, 499, 2608
Ford K. E. S., McKernan B., 2022, MNRAS, 517, 5827
Frank J., Rees M. J., 1976, MNRAS, 176, 633
Generozov A., Perets H. B., 2023, MNRAS, 522, 1763
Generozov A., Stone N. C., Metzger B. D., Ostriker J. P., 2018, MNRAS, 478, 4030
Gezari S., 2021, ARA&A, 59, 21
Goldreich P., Sari R., 2003, ApJ, 585, 1024
Goodman J., Tan J. C., 2004, ApJ, 608, 108
Graham M. J., Djorgovski S. G., Drake A. J., Stern D., Mahabal A. A., Glikman E., Larson S., Christensen E., 2017, MNRAS, 470, 4112
Hamers A. S., Bar-Or B., Petrovich C., Antonini F., 2018, ApJ, 865, 2
Hawkins M. R. S., 1993, Nature, 366, 242
Hayasaki K., Zhong S., Li S., Berczik P., Spurzem R., 2018, ApJ, 855, 129
Hopman C., Alexander T., 2006, ApJ, 645, 1152
Jeans J. H., 1913, MNRAS, 74, 109
Jeans J. H., 1916, MNRAS, 76, 567
Jermyn A. S., Dittmann A. J., Cantiello M., Perna R., 2021, ApJ, 914, 105
Kawaguchi T., Mineshige S., Umemura M., Turner E. L., 1998, ApJ, 504, 671
Kocsis B., Tremaine S., 2011, MNRAS, 412, 187
Kormendy J., Ho L. C., 2013, ARA&A, 51, 511
Kremer K., Lu W., Rodriguez C. L., Lachat M., Rasio F. A., 2019, ApJ, 881, 75
Kremer K., Lombardi James C. J., Lu W., Piro A. L., Rasio F. A., 2022, ApJ, 933, 203
Levin Y., 2007, MNRAS, 374, 515
Li J., Dempsey A. M., Li H., Lai D., Li S., 2023, ApJ, 944, L42
Lightman A. P., Shapiro S. L., 1977, ApJ, 211, 244
Lopez Martin J., Batta A., Ramirez-Ruiz E., Martinez I., Samsing J., 2019, ApJ, 877, 56
Magorrian J., Tremaine S., 1999, MNRAS, 309, 447
McKernan B., Ford K. E. S., Kocsis B., Lyra W., Winter L. M., 2014, MNRAS, 441, 900
McKernan B., Ford K. E. S., Callister T., Farr W. M., O'Shaughnessy R., Smith R., Thrane E., Vajpeyi A., 2022a, MNRAS, 514, 3886
McKernan B., Ford K. E. S., Cantiello M., Graham M., Jermyn A. S., Leigh N. W. C., Ryu T., Stern D., 2022b, MNRAS, 514, 4102
Merloni A. et al., 2015, MNRAS, 452, 69
Merritt D., 2013, Dynamics and Evolution of Galactic Nuclei. Princeton Univ. Press, Princeton
Merritt D., Poon M. Y., 2004, ApJ, 606, 788
Metzger B. D., Stone N. C., 2016, MNRAS, 461, 948
Mikkola S., Aarseth S. J., 1993, Celest. Mech. Dyn. Astron., 57, 439
Murase K., Kashiyama K., Mészáros P., Shoemaker I., Senno N., 2016, ApJ, 822, L9
Nasim S. S. et al., 2023, MNRAS, 522, 5393
Nenkova M., Sirocky M. M., Nikutta R., Ivezić Ž., Elitzur M., 2008, ApJ, 685, 160
Neumayer N., Seth A., Böker T., 2020, A&AR, 28, 4
Noda H., Done C., 2018, MNRAS, 480, 3898
Penston M. V., Perez E., 1984, MNRAS, 211, 33P
Perets H. B., Li Z., Lombardi James C. J., Milcarek Stephen R. J., 2016, ApJ, 823, 113
Perna R., Lazzati D., Cantiello M., 2021a, ApJ, 906, L7
Perna R., Tagawa H., Haiman Z., Bartos I., 2021b, ApJ, 915, 10
Phinney E. S., 1989, in Morris M., ed., Proc. IAU Symp. 136, The Center of the Galaxy. Kluwer Academic Publishers, Dordrecht, p. 543
Rauch K. P., Ingalls B., 1998, MNRAS, 299, 1231
Rauch K. P., Tremaine S., 1996, New Astron., 1, 149
Rees M. J., 1988, Nature, 333, 523
Rowan C., Boekholt T., Kocsis B., Haiman Z., 2023, MNRAS, 524, 2770
Ryu T., Krolik J., Piran T., Noble S. C., 2020, ApJ, 904, 101
Ryu T., Perna R., Wang Y.-H., 2022, MNRAS, 516, 2204
Ryu T., Valli R., Pakmor R., Perna R., de Mink S. E., Springel V., 2023a, MNRAS, 525, 5752
Ryu T., Perna R., Pakmor R., Ma J.-Z., Farmer R., de Mink S. E., 2023b, MNRAS, 519, 5787
Ryu T., de Mink S., Farmer R., Pakmor R., Perna R., Springel V., 2024a, MNRAS, 527, 2734
Ryu T., McKernan B., Ford K. E. S., Cantiello M., Graham M., Stern D., Leigh N. W. C., 2024b, MNRAS, 527, 8103
Samsing J. et al., 2022, Nature, 603, 237
Secunda A., Bellovary J., Mac Low M.-M., Ford K. E. S., McKernan B., Leigh N. W. C., Lyra W., Sándor Z., 2019, ApJ, 878, 85
Secunda A., Hernandez B., Goodman J., Leigh N. W. C., McKernan B., Ford K. E. S., Adorno J. I., 2021, ApJ, 908, L27
Shakura N. I., Sunyaev R. A., 1973, A&A, 500, 33
Shapovalova A. I., Popović L. Č., Burenkov A. N., Chavushyan V. H., Ilić D., Kovačević A., Bochkarev N. G., León-Tavares J., 2010, A&A, 509, A106
Sirko E., Goodman J., 2003, MNRAS, 341, 501
Stern D. et al., 2018, ApJ, 864, 27
Stone N. C., Metzger B. D., 2016, MNRAS, 455, 859
Stone N. C., Metzger B. D., Haiman Z., 2017, MNRAS, 464, 946
Stone N. C. et al., 2020, Space Sci. Rev., 216, 35
Tanaka H., Ward W. R., 2004, ApJ, 602, 388
Tagawa H., Haiman Z., Bartos I., Kocsis B., 2020, ApJ, 899, 26
Tagawa H., Kocsis B., Haiman Z., Bartos I., Omukai K., Samsing J., 2021a, ApJ, 907, L20
Tagawa H., Kocsis B., Haiman Z., Bartos I., Omukai K., Samsing J., 2021b, ApJ, 908, 194
Thompson T. A., Quataert E., Murray N., 2005, ApJ, 630, 167
van Velzen S., 2018, ApJ, 852, 72
Wang Y.-H., Perna R., Armitage P. J., 2021a, MNRAS, 503, 6005
Wang Y.-H., Leigh N. W. C., Liu B., Perna R., 2021b, MNRAS, 505, 1053
Wang Y.-H., McKernan B., Ford S., Perna R., Leigh N. W. C., Mac Low M.-M., 2021c, ApJ, 923, L23
Wang Y.-H., Lazzati D., Perna R., 2022, MNRAS, 516, 5935
Wang Y., Zhu Z., Lin D. N. C., 2023a, MNRAS, 528, 4958
Wang Y., Ford S., Perna R., McKernan B., Zhu Z., Zhang B., 2023b, MNRAS, 523, 2014
Wang Y., Zhu Z., Lin D. N. C., 2024, ApJL, 962, L7
Xin C., Haiman Z., Perna R., Wang Y., Ryu T., 2024, ApJ, 961, 149

Yang Y., Bartos I., Fragione G., Haiman Z., Kowalski M., Márka S., Perna R., Tagawa H., 2022, ApJ, 933, L28
Zhu J.-P., Zhang B., Yu Y.-W., Gao H., 2021, ApJ, 906, L11

APPENDIX A: INITIAL ORBITAL ANGULAR DISTRIBUTION OF RETROGRADE STARS

The distribution of angular momentum can be parametrized by a power-law index, denoted as α, where $p(L) \propto L^{\alpha}$. This parametrization leads to an eccentricity distribution described by $p(e) \propto e(1 - e^2)^{(\alpha - 1)/2}$. When α equals 1, known as the thermal distribution, the eccentricity distribution simplifies to $p(e) \propto e$. For values of α less than 1, the distribution becomes superthermal, indicating that the eccentricity is predominantly high. It can be seen that for any value of α less than or equal to -1, the distribution function $p(e)$ becomes divergent, with the integral of $p(e)$ from 0 to 1 approaching infinity. This suggests that the distribution effectively becomes a delta-like function, specifically $\delta(e = 1)$.

Notably, $\alpha = 0$, which corresponds to a uniform distribution of angular momentum, is the last superthermal distribution with an integrable integer value of α over the range of e from 0 to 1. Since retrograde orbits in the fast inspiral regime will inevitably enter the tidal radius, akin to $\delta(e = 1)$, any integer value of α less than 0 results in the same TDE rate. The $\alpha = 0$ distribution is the most convenient for sampling and provides a lower limit for the TDE rate in this regime. Therefore, we selected this distribution. However, it is important to acknowledge that determining the true value of α for the fast inspiral regime requires extensive hydrodynamic simulations and is sensitive to the specific accretion disc model used. With that in mind, and since any value of α less than or equal to 1 yields the same effective TDE rate, adopting $\alpha = 0$ in this paper, which yields a lower limit to the TDE rate, should be reasonable.

This paper has been typeset from a TEX/LATEX file prepared by the author.